# Physically based Simulation of Twilight Phenomena

JÖRG HABER MARCUS MAGNOR HANS-PETER SEIDEL
MPI Informatik, Saarbrücken, Germany

We present a physically based approach to compute the colors of the sky during the twilight period before sunrise and after sunset. The simulation is based on the theory of light scattering by small particles. A realistic atmosphere model is assumed, consisting of air molecules, aerosols, and water. Air density, aerosols, and relative humidity vary with altitude. In addition, the aerosol component varies in composition and particle size distribution. This allows us to realistically simulate twilight phenomena for a wide range of different climate conditions. Besides considering multiple Rayleigh and Mie scattering, we take into account wavelength-dependent refraction of direct sunlight as well as the shadow of the Earth. Incorporating several optimizations into the radiative transfer simulation, a photo-realistic hemispherical twilight sky is computed in less than two hours on a conventional PC. The resulting radiometric data is useful, for instance, for high-dynamic range environment mapping, outdoor global illumination calculations, mesopic vision research and optical aerosol load probing.

Categories and Subject Descriptors: I.3.7 [**Computer Graphics**]: Three-Dimensional Graphics and Realism—*Color, Shading, Radiosity*; I.6.3 [**Simulation and Modeling**]: Applications; J.2 [**Physical Sciences and Engineering**]: Astronomy, Earth and atmospheric sciences

General Terms: Algorithms

Additional Key Words and Phrases: physics-based sky model, twilight phenomena, refraction, multiple scattering, 3D radiative transfer equation

## 1. INTRODUCTION

> *"The air enwinds the landscape with a wonderful opalescent aura of colors. Without air, light and shadow would clash coldly and callously and luridly as they do on the Moon. In all parts of the Earth, the colors of the air are the same in their regular as well as divergent appearances. ... The subtle color nuances, the mellow blue, the blue afield, the distance of the sky behind the mountains—everything is expressed in a wonderful beauty and a magnificent aura of colors."*
>
> A. Heim (1912)

These lines have not been taken from a poem, but from the introduction to a scientific textbook [Heim 1912]. After this poetic beginning, the author develops a scientific theory of the colors of the sky. Unfortunately, at that time little was known about the structure and content of the Earth's atmosphere. Thus, the scientific relevance of this beautifully illustrated book has turned into a historic one. A similar fate befell another textbook [Gruner and Kleinert 1927] which describes twilight phenomena such as the *bright glow*, the *purple light*, and the *afterglow* based on meteorological assumptions that have become—at least partially—obsolete. Despite the outdated scientific content of these books, the fascination and reverence for the colors of the sky prevailing in these "historic" documents is still alive and valid today.

Modern technological advances such as lidar, satellite imaging, and weather balloons have helped to understand the structure of the atmosphere much better. In addition, precise optical measurements have

Authors' address: MPI Informatik, Stuhlsatzenhausweg 85, 66123 Saarbrücken, Germany.
Email: haberj@acm.org, magnor@mpi-inf.mpg.de, hpseidel@mpi-inf.mpg.de

Fig. 1. Various twilight phenomena simulated with our system for different times and climates. Left to right: *horizontal stripes* appear a few minutes after sunset (sun elevation $-0.5°$ below the horizon, maritime climate); *purple light* is at its strongest about 20–30 minutes after sunset (sun elevation $-3°$, continental climate); *afterglow* shows up about 40–45 minutes after sunset (sun elevation $-6°$, continental climate). Nomenclature of twilight phenomena according to [Minnaert 1999].

been performed to determine the scattering properties of air molecules and aerosols. It is due to these two atmospheric constituents that we perceive the twilight sky in such diverse and changing colors, ranging from deep blue over all shades of purple, orange, and yellow up to blazing red.

Rendering outdoor scenes almost always includes vistas of the sky. So far, either actual photographs or parametric skylight models had to be used for that purpose. But especially for twilight daytimes with their attractive, quickly changing and diverse lighting conditions, no suitable sky modeling tool has been available. In particular, for animations of a sunrise/sunset, standard photographs/video cannot reproduce the dynamic range of the sky while HDR images might be problematic to acquire in the short time of constant sky colors, and parametric models cannot always deliver the subtle nuances of twilight phenomena.

The presented work aims at filling this gap by proposing a method to synthesize realistic images of the sky from its physical causes. It is applicable to any climate, a wide range of meteorological conditions (excluding only completely overcast skies), arbitrary atmospheric pollution and dust concentration, and specifically to any time of the day. The output of our system can be used in either of the following ways:

—direct rendering of outdoor scenes;

—computing global illumination for indoor scenes with natural light entering through doors or windows;

—finding optimal parameters for well-known parametric models, e.g. [Preetham et al. 1999; Dobashi et al. 1997; Tadamura et al. 1993], to achieve realistic sky renderings for a wide variety of atmospheric conditions and times of day. This can be achieved by using our physically based simulations as ground truth in an optimization approach that computes optimal (non-physically based) parameters for any parameteric model by comparision of the predicted result.

Our simulations are based on physical laws in conjunction with physical parameters that have been actually measured for different climate conditions, taking into account

—solar irradiance spectrum and its absorption in the ozone layer,

—wavelength-dependent refraction of direct sunlight in the atmosphere,

—climate-dependent composition and size distribution of aerosols / dust particles,

—height-dependent air, humidity, and aerosol density,

—Rayleigh scattering (air molecules) and Mie scattering (aerosols),

—radiative transfer (multiple scattering), as well as

—the shadow of the Earth.

To calculate the optical characteristics of the atmosphere for any given aerosol mixture, density, particle size distribution, and humidity, we make use of the publicly available OPAC software package [Hess et al. 1998; Hess 1998] which was originally developed for meteorological and climate simulations.

## 2. PREVIOUS WORK

The colorful skies during a cloudless sunset have spurred not only the imagination of countless poets but also the curiosity of generations of scientists. In a qualitative way, the correlation between twilight colors and atmospheric conditions has probably been recognized very long ago: country sayings and farmer almanacs gave rules to forecast the weather from twilight colors long before the invention of the barometer. A quantitative explanation, however, eluded even early 20th century scientists [Gruner and Kleinert 1927; Heim 1912; Minnaert 1999; Rozenberg 1966] who also couldn't give much more than a description of twilight phenomena. Today, the underlying physical laws leading to the colors at twilight are well known. A modern, high-level description of twilight phenomena is given in the textbook by Lynch and Livingston [2001]. Van de Hulst rigorously derives the scattering characteristics of single particles [1982], and Chandrasekhar's radiative transfer theory lays the foundation to describe multiple scattering [1950]. Several decades later, the first computers became powerful enough to enable quantitative investigations of how colors during twilight depend on atmospheric conditions.

In essence, we must solve the 3D rendering equation [Kajiya 1986]. Looking for standard radiosity methods, reproducing faithful twilight colors poses some specific difficulties. First, neither single scattering nor the diffusion limit are permissible approximations for light transport in the twilight atmosphere [Nagel et al. 1978]: twilight colors are the result of a finite number of multiple scattering events. Second, the atmosphere is almost transparent, and all regions of the directly illuminated atmosphere receive similar amounts of sunlight. This renders radiosity methods based on biasing the simulation, for instance importance sampling [Shirley 1990] or progressive radiosity [Cohen et al. 1988], inefficient since all regions are of about equal importance for the result. Furthermore, an atmosphere volume of tens of millions of cubic kilometers around the observer contributes to the appearance of the sky. This volume is not orthogonal (due to Earth's curvature), and absorption and scattering characteristics vary within the volume. Thus, in direct Monte-Carlo methods, most simulated photons are wasted, resulting in only sparse distribution information and grainy sky appearance, even though the actual twilight sky colors vary smoothly [Blattner et al. 1974].

During the past decades, a large body of literature was published on atmospheric optics. While a lot of computer experiments were conducted in climatology to investigate global radiative transfer, only a handful of publications are concerned with the visual aspects of twilight colors, mainly to remotely probe atmospheric constituents and aerosol density [Bigg 1956; Shah 1970; Jadhav and Londhe 1992; Belikov 1996]. To compute the radiance observed at a single point on the Earth's surface during twilight, numerical simulations have been performed by various authors. Dave and Mateer [1968] show colorimetry results for five atmospheric models, but do not take into account multiple scattering and atmospheric refraction. The model proposed by Adams *et al.* [1974] includes refraction, but still uses single scattering only. Due to the early year of publication, results are presented as tables and diagrams rather than visualizations. Some early attempts at simulating twilight phenomena can also be found in the applied optics and planetology literature [Blattner et al. 1974; Anderson 1983].

In computer graphics, a number of researchers have concerned themselves with realistic sky visualization. A system to render the night sky in all its splendor was presented by Wann Jensen *et al.* [2001]. For daylight sky rendering, two different approaches have been pursued [Sloup 2002]: phenomenological models describe sky appearance in terms of non-physical parameters, while physics-based systems solve the 3D rendering equation known as *radiative transfer* based on actual atmospheric conditions. An analytical model that can be fit to actual observational data or simulation results of daytime sky appearance is presented in [Preetham

et al. 1999]. A series expansion of specific sky data was proposed by Dobashi *et al.* [1997]. Similarly, steerable basis functions were employed in [Nimeroff et al. 1996]. Tadamura *et al.* use a skylight model for outdoor renderings [1993]. These empirical sky light models typically rely on actually recorded images of the sky or use the CIE standard on daylight luminance distribution [CIE-110-1994 1994]. Their goal is to provide fast algorithms for rendering a subjectively plausible day or nighttime sky.

To compute accurate sky appearance from its physical causes, Klassen describes atmospheric scattering and refraction in suitable form for numerical simulations [1987]. Irwin presents results for a system that considers Rayleigh scattering from air molecules [1996]. Anisotropic scattering from aerosols is taken into account by Nishita *et al.* [1996] as well as by Jackel and Walter [1997]. Both papers also take double scattering into account. Nishita *et al.* [1996] employ the two-pass method first formulated by Kajiya and Herzen [1984]. Their approach is built upon the work by Rushmeier and Torrance [1987] and Max [1994]. Jackel and Walter [1997], on the other hand, introduce an extinction correction term and use a simplified second-order scattering model. While both papers also present results for times when the Sun is below the horizon, these images must be considered a rough approximation to the true sky colors after sunset. To obtain the correct sky illumination during twilight, among other things, higher-order scattering events need to be taken into account [Blattner et al. 1974; Anderson 1983; Ougolnikov and Maslov 2002].

We describe an approach how to compute the full radiative transfer in the atmosphere within reasonable computation times to correctly model all effects that influence sky appearance when the Sun is above as well as below the visible horizon. This work intends to fill the gap between realistic/physical daytime [Preetham et al. 1999; Nishita et al. 1996] and night [Wann Jensen et al. 2001] sky rendering.

## 3. OVERVIEW

Computing the colors of the sky for an arbitrary observer position and observation date and time is performed in five steps:

(1) Compute the position of the Sun from the observer position and the observation date and time.
(2) Set up the atmosphere model and initialize all wavelength-dependent optical parameters.
(3) Compute the direct illumination contribution of the atmosphere from the Sun taking into account atmospheric refraction, the ozone layer, and the shadow of the Earth.
(4) Compute the indirect illumination contribution by simulating multiple scattering events.
(5) Convert the illuminated atmosphere into an RGB "sky texture" as seen from the observer.

*Astronomical Computations.* We compute the position of the Sun according to the observer's longitude and latitude and the date and time of the observation using the expressions given in [Meeus 1988; 1999]. Similar formulas have been presented by Wann Jensen *et al.* [2001].

*Setting up the Atmosphere.* Our atmosphere model consists of atmosphere layers and atmosphere cells (Section 4.1). All computations are performed for a number $N_\lambda$ of wavelengths $\lambda_i$ set by the user. Wavelength samples need not be distributed equidistantly over the color spectrum. Typically, we specify eight samples covering the wavelength range of visible light (380 nm – 720 nm). We precompute for each wavelength the optical parameters of the atmosphere using the publicly available OPAC software package (Section 4.1.1). Spectral solar irradiance (Section 4.2), ozone absorption (Section 4.3), local index of refraction (Section 4.4), scattering by air molecules (Section 4.5.1) as well as extinction, scattering, and scattering anisotropy due to aerosols (Section 4.5.2) are taken into account. For tabulated parameter values, we linearly interpolate the corresponding value for each wavelength $\lambda_i$ from neighboring entries in the tables.

*Direct Illumination.* All atmosphere cells not in the shadow of the Earth receive direct sunlight (see Section 4.1). Solar irradiance (Section 4.2) is filtered by the ozone layer (Section 4.3), refracted by air

molecules (Section 4.4), and scattered by air molecules and aerosols (Section 4.5) on its way through the atmosphere. After this initial step, each atmosphere cell that does not lie in the shadow of the Earth stores the radiant power it has received from the Sun.

*Indirect Illumination.* This stage takes into account multiple scattering between atmosphere cells (Section 4.5.3). It is by far the computationally most expensive step. A naïve implementation can easily exceed computation times of several days. In Section 5 we thus present several algorithmic optimizations and permissible approximations to reduce the computation times for images such as the ones shown throughout this paper to about 1–2 hours.

*Sky Texture.* Finally, we create a *sky texture*, equivalent to an environment map, which holds the colors of the sky as seen from the observer's position in any direction of the hemisphere (Section 4.7). For final rendering, the spectral information is converted to RGB color space. We convert the sampled spectral distribution into its corresponding XYZ color by convolution with the CIE (1964) 10° color matching functions. Next, we convert from XYZ to RGB color space using the sRGB primaries from CIE Rec. 709 and a D65 whitepoint. Details of spectral conversion can be found in [Wyszecki and Stiles 1982] or in [Hall 1989].

## 4. SIMULATION

In this section, we describe the physical and meteorological background of our simulations and give details on the implementation. For an efficient implementation, however, several optimizations have to be included. These optimizations are described in Section 5.

### 4.1 Atmosphere Model

Our atmosphere model consists of two sets of distinct building blocks: a set of *atmosphere layers* and a set of *atmosphere cells*. Atmosphere layers are used to store optical properties of the atmosphere, while atmosphere cells are used during radiative transfer computations.

4.1.1 *Optical Characteristics.* The optical properties of the atmosphere depend in a non-trivial way on climate conditions, local humidity and altitude. We do not attempt to model these complex relationships ourselves. Instead, we use the publicly available OPAC software package [Hess 1998], described in detail in [Hess et al. 1998], to compute the wavelength-dependent aerosol absorption coefficient $\sigma_a^{\text{aerosol}}(\lambda)$, scattering coefficient $\sigma_s^{\text{aerosol}}(\lambda)$, and anisotropy factor $g(\lambda)$ (see Section 4.5). OPAC computes these optical properties for any arbitrary aerosol composition, particle size distribution and humidity. Typical aerosol mixtures and height profiles for a variety of different climates are also provided by OPAC. At sea level, the aerosol extinction coefficient $\sigma_e^{\text{aerosol}}(\lambda) = \sigma_a^{\text{aerosol}}(\lambda) + \sigma_s^{\text{aerosol}}(\lambda)$ typically ranges from 0.02–0.4 $\text{km}^{-1}$, while the anisotropy factor $g$ varies between 0.5–0.8.

The wavelength-dependent scattering coefficient of air molecules is taken from tables in [Nagel et al. 1978]. Unlike aerosols, pure air does not significantly absorb visible light. Thus, the extinction coefficient of air $\sigma_e^{\text{air}}$ can safely be assumed identical to the scattering coefficient, $\sigma_e^{\text{air}}(\lambda) = \sigma_s^{\text{air}}(\lambda)$. The local index of refraction of the atmosphere is computed as described in Section 4.4.

4.1.2 *Atmosphere Layers.* We model the atmosphere around the Earth up to a height of $H_{\max} = 35\,\text{km}$. Above this upper boundary of the stratosphere, there are no more particles or sufficiently many air molecules to affect our calculations, only the ozone layer which simply filters the incoming sunlight. We discretize the atmosphere into a set of geocentric atmosphere layers $L_i, (i = 1, \ldots, N)$. Each layer $L_i$ has an individual upper and lower boundary at height $H_{i,\max}$ and $H_{i,\min}$, respectively, with no gaps between adjacent layers:

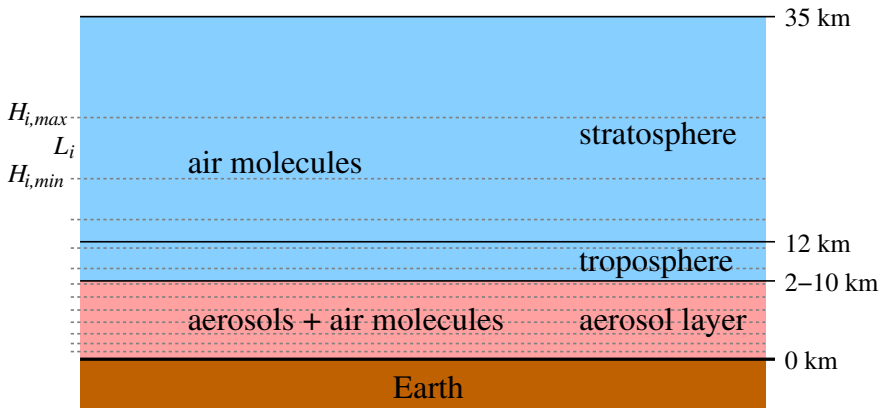


Fig. 2. Cross-section of the atmosphere model with atmospheric layers (dotted lines). Decomposition into aerosol-containing region, clear troposphere, and stratosphere according to [Hess et al. 1998]. The height of the aerosol region depends on the climate.

$H_{i,\min} = H_{i-1,\max}, (i = 2, \ldots, N)$, see Figure 2. The thickness $D_i$ and center height $H_i^*$ of layer $L_i$ then is

$$D_i \;=\; H_{i,\max} \;-\; H_{i,\min}\;, \qquad H_i^* \;=\; \frac{1}{2}\,(H_{i,\max} \;+\; H_{i,\min})\;.$$

Each layer $L_i$ is assigned a relative humidity $w_i$ and the following optical attributes:

—aerosol scattering coefficient $\sigma_{s,i}^{\text{aerosol}}(\lambda)$ and extinction coefficient $\sigma_{e,i}^{\text{aerosol}}(\lambda) = \sigma_{s,i}^{\text{aerosol}}(\lambda) + \sigma_{a,i}^{\text{aerosol}}(\lambda)$;
—Henyey-Greenstein scattering anisotropy coefficient $g_i(\lambda)$;
—isotropic scattering coefficient of air $\sigma_{s,i}^{\text{air}}(\lambda)$;
—index of refraction $\eta_i(\lambda)$.

These parameters are functions of the wavelength $\lambda$ and are evaluated for a discrete set of $\lambda_j, (j = 1, \ldots, N_\lambda)$.

Discretizing the atmosphere into individual layers $L_i$ allows us to model the variation of optical parameter values with altitude. To account for the exponential fall-off of particle density with height, we compute for each layer $L_i$ the following factors:

$$z_i^{\text{aerosol}}(H_i^*) \;=\; \exp(-H_i^*/Z)\;, \qquad z_i^{\text{air}}(H_i^*) \;=\; \exp(-H_i^*/8)\;.$$

For aerosols, the scale height parameter $Z$ depends on the climate and is provided by OPAC. In each layer $L_i$, we multiply the extinction and scattering coefficients with the corresponding factor $z_i^{\text{aerosol}}$ and $z_i^{\text{air}}$. The height dependence of the index of refraction is already incorporated in the equations in Section 4.4.

Since optical properties are assumed constant within each layer $L_i$, we distribute the layers such that each layer contains approximately the same number $M$ of air molecules:

$$\int_{H_{i,\min}}^{H_{i,\max}} \mathrm{e}^{-h/8}\,\mathrm{d}h \;\stackrel{!}{=}\; M \;:=\; \frac{1}{N}\int_{H_{0,\min}}^{H_{N,\max}} \mathrm{e}^{-h/8}\,\mathrm{d}h \qquad \forall\, i = 1, \ldots, N\;.$$

Substituting $H_{i,\max}$ with $H_{i+1,\min}$, we obtain the recursive definition

$$H_{i+1,\min} \;=\; -8 \cdot \ln\left(\mathrm{e}^{-H_{i,\min}/8} \;-\; M/8\right)\;, \qquad i = 1, \ldots, N-1\;,$$

where the lower height of layer $L_1$ is initialized to zero, $H_{1,\min} := 0\,\text{km}$, and the top height of the last layer is set to the upper boundary of our atmosphere model, $H_{N,\max} := H_{\max} = 35\,\text{km}$. The computation of the

optimal distribution of layers is performed automatically during initialization for a user-specified number of layers $N$. For our simulations, we typically use 20–50 layers.

4.1.3 *Atmosphere Cells.* Atmosphere cells are set up in the *local horizontal coordinate system*: the origin is given by the observer position, and the normal to the Earth's surface at the observer represents the $z$-axis. To be able to later exploit the symmetry of the problem, we let the $x$-axis always point towards the azimuthal direction of the Sun. We discretize the atmosphere in small volumes denoted atmosphere cells $C_k$. These cells are created by uniformly dividing a set of *shells* along azimuth and height. Shells are located concentrically about the origin of the local horizontal coordinate system, see Figure 3. In this spherical parametrization, each cell $C_k$ is described by its spherical coordinates azimuth $\phi_{k,\min/\max} \in [-180°, 180°]$ height and $\psi_{k,\min/\max} \in [-90°, 90°]$ and its radius $r_{k,\min/\max} \in [R_\epsilon, R_{\max}]$. Thus, each cell $C_k$ spans the volume

$$V_k \;=\; [r_{k,\min}, r_{k,\max}] \times [\phi_{k,\min}, \phi_{k,\max}] \times [\psi_{k,\min}, \psi_{k,\max}] \; .$$

The spherical coordinates of the center $C_k^*$ of a cell $C_k$ are set to

$$C_k^* \;=\; \left( \frac{r_{k,\min} + r_{k,\max}}{2}, \frac{\phi_{k,\min} + \phi_{k,\max}}{2}, \frac{\psi_{k,\min} + \psi_{k,\max}}{2} \right) \; .$$

Any cell whose center is above the Earth's surface is used for simulation, i.e. also cells below the visible horizon participate.

A lower boundary $R_\epsilon$ of the radius has been chosen to avoid cells with a degenerated shape at the origin. In our simulations we use $R_\epsilon = 10\text{m}$. The upper boundary $R_{\max}$ is chosen such that the part of the atmosphere that is still directly illuminated by the Sun during astronomical twilight (i.e. when the Sun is up to 18° below the horizon) is included in the hemisphere around the observer. With $R_{\text{Earth}} = 6371\,\text{km}$ being the radius of the Earth we obtain $R_{\max} = \sqrt{H_{\max}^2 + 2R_{\text{Earth}}H_{\max}} \approx 670\,\text{km}$.

To minimize later approximation errors, we found it beneficial if the atmosphere cells have the same dimension along radial and vertical direction. We therefore compute the number of shells and the individual thickness of each shell from a given number $S$ of azimuthal subdivisions. First, we set the identical angular subdivision for the height (i.e. $\psi_{k,\max} - \psi_{k,\min} = \phi_{k,\max} - \phi_{k,\min}$ for all cells $C_k$). Next, we compute the thickness $r_{j,\max} - r_{j,\min}$ of each shell $j$ to match the average arc length of the (curved) edges of the cells in that shell (see Figure 4):

$$r_{j,\max} \;=\; r_{j-1,\max} \;+\; \frac{1}{2}(b_{j-1} + b_j) \, .$$

With the arc length defined as $b_j := \alpha \cdot r_{j,\max}$, it follows that

$$r_{j,\max} \cdot (1 - \frac{\alpha}{2}) \;=\; r_{j-1,\max} \cdot (1 + \frac{\alpha}{2})$$

and we obtain the geometric sequence:

$$r_{j,\max} \;=\; R_\epsilon \cdot q^j \, , \qquad q := \frac{1 + \alpha/2}{1 - \alpha/2} \, , \;\; \alpha := \frac{360°}{S} \; .$$

We compute and set up as many shells as fit into the interval $[R_\epsilon, R_{\max}]$, i.e. until $r_{j,\max} >= R_{\max}$. In practice, this mechanism yields 101 shells for $S = 72$ (5° angular subdivision) and 252 shells for $S = 180$ (2° subdivision). This way, we make sure that each cell has the same length in radial as well as height direction. Cell size, of course, varies strongly between the innermost and the outermost shell, which must be taken into account during radiative transfer computation.

During initialization, we store for each cell $C_k$ its center position $C_k^*$ and volume $V_k$ as well as the index $i$ of the atmosphere layer $L_i$ that contains $C_k^*$.

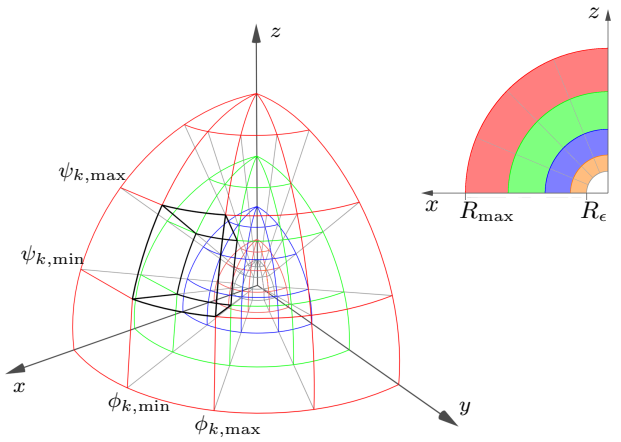


Fig. 3. Spherical parametrization of our atmosphere model (one quarter of the hemisphere) with color-coded shells. A single atmosphere cell is drawn with bold lines. Top right: a side view of the $xz$-plane illustrates the layout of the shells. The thickness of the shells is adapted to ensure a relatively uniform cell shape.

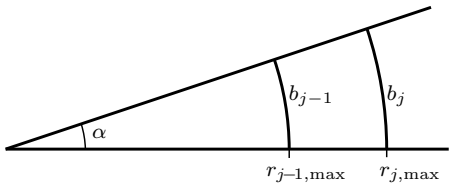


Fig. 4. Cross-section of a single cell with inner radius $r_{j,\min} = r_{j-1,\max}$ and outer radius $r_{j,\max}$. The arc length of the cell's curved edges is denoted by $b_{j-1}$ and $b_j$, respectively.

4.1.4 *Boundary Conditions.* To simulate the propagation of visible light through the atmosphere, we need to take into account what happens to light that reaches the boundaries of our atmospheric volume model. For our simulation, we assume that light reaching the boundary of our model volume is lost. This is definitely true for the upper boundary, since above the stratosphere, no more scattering or absorption takes place, and light escapes freely into outer space without affecting our simulation anymore. Along the circumference of our spherical volume lies more atmosphere that contributes some scattered light to our volume, which we neglect. Two reasons allow us to do so: in daytime regions, the scattered light contribution is many orders of magnitude dimmer than direct sunlight and thus insignificant; along the twilight border, scattered outside light affects those regions within the mean scattering length of the atmosphere, while our volume radius is many times larger than the mean scattering length of the atmosphere; in nighttime regions, outside atmosphere regions do not contribute at all.

As the last boundary, the ground remains. The visible-wavelength albedo of Earth's surface varies considerably, from 3.5% total reflectance for the oceans and 7%-12% for urban areas on to 13% for forests, 15% for farmland soil and up to 90% for freshly fallen snow [Walker ]. Depending on individual ground conditions around the observer, the effect of sunlight reflected off the ground, or even of scattered sky light reflected off fresh snow, can have an impact on overall sky brightness, most pronounced during the day. The ground thereby acts as an undirected area light source, evenly contributing to the illumination of all atmosphere regions. Thus, if isotropic, wavelength-independent ground reflectance is taken into account, the relative amount of radiation received by different atmospheric regions does not change considerably. The sky becomes brighter, but not different in color. So, while our system is easily capable of simulating the effects of arbitrary Earth albedo characteristics, we decided to present here results for a dark ground.

## 4.2 Solar Irradiance

For the initial solar irradiance outside the atmosphere we use the solar spectrum data measured by Kurucz *et al.* [1984] for wavelengths from 200 nm to 1000 nm. This data is given as *spectral irradiance* (denoted as *residual flux* in Kurucz's terminology) in Watts per square meter per nanometer ($\mathrm{W\,m^{-2}\,nm^{-1}}$) and converted to irradiance (in $\mathrm{W\,m^{-2}}$) by integrating over wavelength intervals centered equidistantly at 1 nm sampling

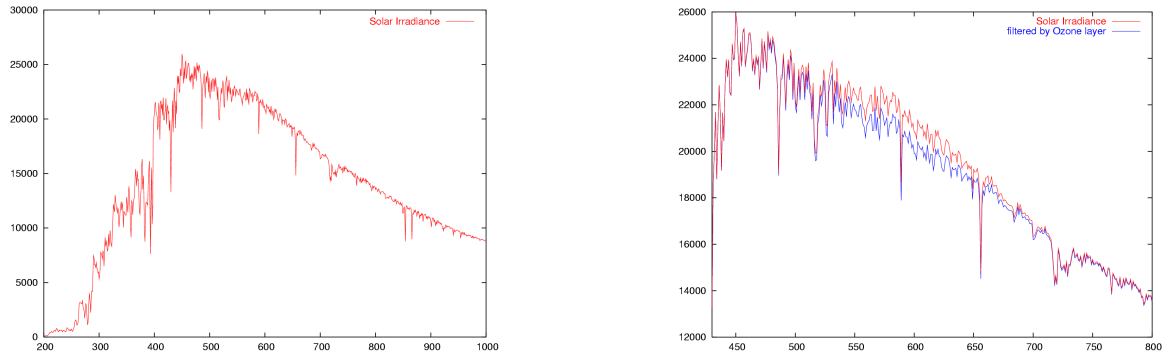


Fig. 5. Left: Spectrum of solar irradiance outside the atmosphere. For wavelength $\lambda$ ranging from 200 nm to 1000 nm, the solar irradiance outside of atmosphere is given in W m$^{-2}$. Data obtained from [Kurucz et al. 1984]. Right: Absorption of solar irradiance in the ozone layer for $\lambda = [430\,\text{nm}, 800\,\text{nm}]$. Outside this wavelength interval, ozone absorption is below 0.1 %. Ozone scattering coefficients taken from [Nagel et al. 1978].

distance, see Figure 5 (left). We model the Sun as a directional light source, a permissible approximation since twilight colors vary more slowly with direction than the Sun disc's diameter of 0.5°.

### 4.3 Absorption in the Ozone Layer

The upper part of the stratosphere (at 35 km) contains significant amounts of ozone which filters out the UV radiation of the incoming sunlight. In addition, ozone exhibits a weak absorption band in the green part of the visible spectrum. The influence of ozone on the colors of the twilight sky has been studied and simulated numerically by Adams *et al.* [1974].

The ozone present in the stratosphere amounts to a layer of approximately 3 mm thickness at normal temperature and pressure (20° C, 1014 hPa). According to [Royal Meteorological Institute of Belgium 2002], the thickness of the ozone layer varies periodically between 2.6 mm and 3.7 mm over the year. Taking into account this annual thickness variation and the wavelength-dependent absorption coefficient $\sigma^{\text{ozone}}(\lambda)$, we compute the filtered solar irradiance as:

$$I_{\text{filtered}}(\lambda) \;=\; I_{\text{unfiltered}}(\lambda) \cdot \exp\left(-\sigma^{\text{ozone}}(\lambda) \cdot d\right) \;.$$

Tabulated values of the ozone absorption coefficient are given in [Nagel et al. 1978]. Figure 5 (right) illustrates the effect of filtering by the ozone layer for $\lambda = [430\,\text{nm}, 800\,\text{nm}]$. Only ozone exhibits non-negligible absorption in the visible spectrum. Other gaseous atmospheric constituents do not attenuate visible light.

### 4.4 Atmospheric Refraction

For direct illumination of cells, we take into account atmospheric refraction. Within each layer $L_i$, the refractive index $\eta_i$ depends on the wavelength $\lambda$, altitude $h$, and the relative humidity $w$. In our atmosphere model, we assume a constant height and humidity within each layer. Thus, for each layer we can precompute and store the indices of refraction for all wavelengths used during our simulation. To compute $\eta_{h,w}(\lambda)$ for height $h$ and humidity $w$, we use the following formulas taken from [Ciddor 1996], where the wavelength $\lambda$ has to be given in micrometers ($\mu$m), the height $h$ in kilometers (km), and the relative humidity $w$ ranging from 0 for dry air to 1 for a saturated (wet) atmosphere:

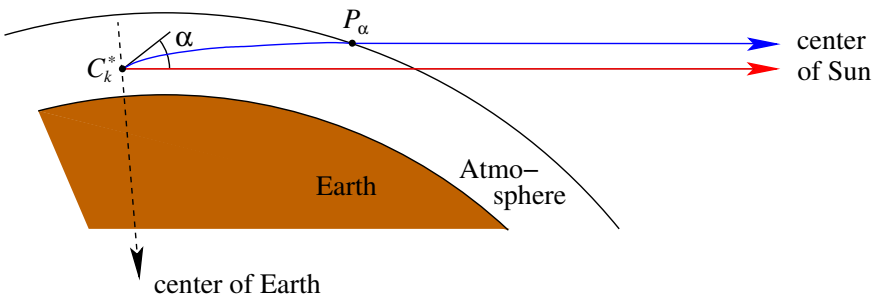


Fig. 6. Refraction of sunlight in the atmosphere (not to scale). Red line: trajectory without refraction. Blue line: refracted trajectory is curved downwards and forms an angle $\alpha$ with the unrefracted trajectory.

$$\eta_{h,w}(\lambda) \;=\; 1 \;+\; e^{-h/8} \cdot ((1-w) \cdot \tilde{\eta}_{\mathrm{dry}}(\lambda) \;+\; w \cdot \tilde{\eta}_{\mathrm{wet}}(\lambda))$$
$$\tilde{\eta}_{\mathrm{dry}}(\lambda) \;=\; \left( \frac{5792105.0}{238.0185 - \lambda^{-2}} \;+\; \frac{167917.0}{57.362 - \lambda^{-2}} \right) \cdot 10^{-8}$$
$$\tilde{\eta}_{\mathrm{wet}}(\lambda) \;=\; \left(295.235 \;+\; 2.6422\,\lambda^{-2} \;-\; 0.03238\,\lambda^{-4} \;+\; 0.004028\,\lambda^{-6}\right) \cdot 1.022 \cdot 10^{-8}$$

Several approaches to compute the trajectory of the refracted ray are discussed in Bruton's dissertation [1996], for instance approximating the trajectory by piecewise parabolas. In contrast, we nonlinearly ray-trace the path of light through the atmosphere. For a given cell center $C_k^*$, we need to find the initial light direction such that the refracted trajectory ends up traveling towards the Sun, see Figure 6. The trajectory of light traveling from the Sun to $C_k^*$ lies in the plane defined by the center of the Sun, the Earth, and the cell center. [1]. For any given cell, we denote as $\alpha$ the sought angle between geometrical and optical Sun direction. In practice, this angle is always smaller than 2 degrees.

We employ a robust and fast iterative algorithm to solve the Eikonal equation (a first order non-linear PDE, mathematically expressing *Fermat's Principle* [Stam and Languenou 1996]) by tracing through the atmosphere layers $L_i$, given the boundary conditions that the trajectory passes through $C_k^*$ and ends up in Sun direction when leaving the atmosphere. For a light ray traveling from layer $L_i$ into the neighboring layer $L_j$ ($j = i \pm 1$), we compute the direction of the refracted light ray according to Snell's law of refraction. The effective index of refraction $\eta$ used in Snell's law is the ratio of the indices of refraction $\eta_i$ and $\eta_j$ of layers $L_i$ and $L_j$, respectively. For the special case of a sun ray entering the top layer $L_N$ of the atmosphere, we use $\eta = 1/\eta_N$.

We exploit the fact that due to the decreasing atmosphere density with altitude, the refracted light trajectory is always curved downward towards the center of the Earth as depicted in Figure 6. The optical trajectory passing through $C_k^*$ forms the (unknown) angle $\alpha$ with the straight line connecting $C_k^*$ and the center of the Sun $C_{\mathrm{Sun}}$. A binary search for $\alpha$ is performed by computing the directional error for a minimal and maximal angle, initialized with $\alpha_{\mathrm{low}} := 0°$ and $\alpha_{\mathrm{high}} := 2°$. The directional error $\epsilon_\alpha$ is computed as

$$\epsilon_\alpha \;=\; 1 \;-\; \left\langle \overrightarrow{C_k^*\, C_{\mathrm{Sun}}},\, \overrightarrow{P_\alpha} \right\rangle ,$$

where $\overrightarrow{C_k^*\, C_{\mathrm{Sun}}}$ expresses the (normalized) direction vector from cell center to the Sun, and $\overrightarrow{P_\alpha}$ is the (normalized) direction vector of the refracted trajectory at point $P_\alpha$ where it leaves the atmosphere. For the

[1] If $C_k^*$ lies on the line from the center of the Sun to the center of the Earth, the plane degenerates into a straight line and no refraction occurs since the the light ray penetrates the atmosphere orthogonally.

correct value of $\alpha$, these directions coincide and the error $\epsilon_\alpha$ becomes zero. The binary search typically converges in 5–15 iterations (depending on the height of the Sun above the horizon) with a remaining error of 0.1° which is considerably smaller than the Sun disc's diameter of 0.5°. Since sky twilight colors vary slowly with direction, the Sun's angular extent can be safely neglected, and we assume directed illumination. At a maximum directional effect of less than 2°, refraction is negligible for isotropic as well as anisotropic re-scattering, which diminishes light directionality.

### 4.5 Scattering

The splendid colors during twilight are caused by scattering of sunlight by the constituents in the atmosphere. Colors come about because the amount of scattering varies with wavelength. Since scattering characteristics depend on particle density, size and material, different atmospheric conditions are responsible for the great variety of twilight color displays.

Atmospheric scattering effects can be separated into two regimes: Rayleigh scattering caused by air molecules, which are orders of magnitude smaller than the wavelengths of visible light, and Mie scattering by aerosol particles (haze, dust, airborne pollutants), whose sizes are approximately of the order of visible light wavelengths. Atmospheric water content can range from molecular size and droplets in clouds up to macroscopic rain drops. Excluding rain and fog, the scattering contribution from atmospheric humidity is already incorporated in the scattering coefficient values calculated by OPAC [Hess et al. 1998].

4.5.1 *Rayleigh Scattering by Air Molecules.* The molecular constituents of the atmosphere are much smaller than the wavelength of visible sunlight, and pure air does not absorb any light in the visible regime. However, the air molecules scatter light, as described by Rayleigh scattering. Each molecule acts as a single minute dipole antenna which absorbs and re-radiates the very much longer electromagnetic light waves. The amount of energy first absorbed and then re-radiated in all directions by a single molecule can be analytically derived from electrodynamic theory [van de Hulst 1982]. Suffice it to state here that the amount of Rayleigh scattering increases with the fourth power of radiation frequency, i.e. the scattering probability for blue light is about 16 times higher than for red light. Actually, the perceived blue color of the clear daytime sky is the result of the combined effects of this fourth-power scattering dependence, the Sun's spectrum, the pitch-dark background of empty space beyond our atmosphere, and the photopic response of the human eye (which prevents us from perceiving the sky as being violet) [Lilienfeld 2004]. For the wavelength-dependent scattering coefficient of pure air $\sigma_s^{\text{air}}(\lambda)$, we use tabulated values taken from [Nagel et al. 1978] which we scale according to each layer's air molecule density (proportional to barometric pressure).

The directional characteristics of Rayleigh scattering depend on incident and outgoing light direction, as well as incoming wave polarization. Since we are concerned here with the appearance of the sky to the naked human eye, which is by and large not polarization-sensitive, we need to regard only the net effect on unpolarized illumination. The directional dependence of scattered light intensity is then proportional to $1+\cos^2\theta$, where $\theta$ is the angle between incoming light direction and outgoing scattered light direction [van de Hulst 1982]. This scattering characteristic suggests a darker region in the sky at 90° from the sun. However, the clear blue sky appears smooth to the naked eye. This observation already indicates the importance and the effect of multiple scattering: The scattered blue sunlight is likely to ungo several more scattering events before reaching the observer on the ground. After the first scattering event, there is no single incoming light direction anymore. The already scattered light arrives from all directions, diminishing in sum the importance of angular scattering dependence. The net angular scattering anisotropy evens out very quickly to become isotropic. Thus, it is safe to approximate the angular dependence of scattering by air molecules as being isotropic [Nagel et al. 1978]. In Sect. 4.6.2, we make use of this characteristics of multiple scattering again to efficiently compute multiple scattering events by aerosols.

4.5.2 *Mie Scattering by Aerosols.* A different matter is scattering by particles of sizes on the order of the incoming light's wavelength. We use the term aerosols to subsume all kinds of airborne atmospheric constituents other than molecules, such as soil dust, microscopic water droplets, pollen, minute sulfur beads, and other solid air pollutants. These particles' surface acts as if being composed of multiple dipoles that all oscillate with different phase when excited by an electromagnetic light wave. Particle size, shape, and dielectric material constant all influence scattering behavior. Mie scattering theory mathematically models the complex scattering characteristics of such particles. Unfortunately, quantitative descriptions can only be stated in form of infinite expansion series [van de Hulst 1982]. As general observations, though, Mie scattering is much less wavelength-dependent than Rayleigh scattering. Instead, it is considerably anisotropic, i.e. light is preferably scattered into the forward direction.

For our purposes, finding valid approximations to the exact Mie scattering expressions is inevitable. To do so, we can exploit the fact that we are dealing with a very large ensemble of atmospheric aerosol particles that is made up of various chemical compounds and a large range of particle sizes and shapes. In addition, the illuminating sunlight is randomly polarized, incoherent and polychromatic. After averaging the exact Mie scattering expressions over the range of particle sizes, shapes, and dielectric constants for incoherent light of arbitrary polarization and a range of wavelengths, the aerosol ensemble's net scattering characteristics can be expressed by three coefficients [Hess et al. 1998]: scattering by a mixture of aerosols can be modeled by the mean scattering and extinction coefficients $\sigma_s^{\text{aerosol}}(\lambda)$, $\sigma_e^{\text{aerosol}}(\lambda)$, and the mean scattering anisotropy $g(\lambda)$. In optics as well as climate research, scattering anisotropy is typically modeled using the Henyey-Greenstein expression

$$I(\lambda,\theta) \;\approx\; I_1^{\text{anisotr}}(\lambda) \cdot \frac{1}{4\pi} \frac{1-g(\lambda)^2}{(1+g(\lambda)^2-2g(\lambda)\cos\theta)^{3/2}} \cdot \Delta\omega \tag{1}$$

where $\theta$ is the phase angle (i.e. the angle between incident light and scattering direction), $g(\lambda)$ is the anisotropy parameter, and $\Delta\omega$ denotes the scattering cone's solid angle. $\sigma_s^{\text{aerosol}}(\lambda)$, $\sigma_e^{\text{aerosol}}(\lambda)$ and $g(\lambda)$ can be calculated for any given aerosol mixture, particle size distribution, relative humidity and altitude using the OPAC software package [Hess 1998].

4.5.3 *Multiple Scattering.* Twilight colors are substantially influenced by light scattered many times and over long distances. With the Sun below the horizon, only high-altitude and distant atmospheric regions in sunset direction still receive direct sunlight. The rest of the atmosphere only receives indirect, multiply scattered light.

The challenge in simulating the radiative transfer in the atmosphere consists of keeping computation times as well as memory requirements to manageable levels. Fortunately, as we have seen above, multiple scattering quickly diminishes the influence of scattering anisotropy. To model multiple scattering through anisotropic media, it is common practice in optics research [Magnor et al. 2001] to approximate each scattering event as being isotropic with an effective scattering coefficient

$$\overline{\sigma}_s^{\text{aerosol}}(\lambda) \;=\; (1-g(\lambda)) \cdot \sigma_s^{\text{aerosol}}(\lambda). \tag{2}$$

In our system, instead of approximating Mie scattering as being isotropic right from the start, we do take into account anisotropic scattering for the first scattering event. This way, we retain the influence of anisotropic scattering for the strongest, directional illumination contribution from direct sunlight. Only the indirect, non-directional illumination from already scattered light is further scattered isotropcially using the effective scattering coefficient. This approach allows us to accurately simulate the effect of Mie scattering while greatly reducing computation time as well as required storage capacity, since no directional information must be stored anymore after the first scattering event.

### 4.6 Radiative Transfer

To calculate the distribution of radiant power in the atmosphere, we first need to determine the amount of direct sunlight received by each atmosphere cell. Subsequently, we simulate the exchange of scattered light between all cells: We regard each cell as the source cell $C_{\text{src}}$ that radiates its scattered light towards all other cells, denoted target cells $C_{\text{tgt}}$. Two nested loops go over all cells, and it is at this core of our simulation that the implementation must be as efficiently a possible (Section 5).

For the sake of presentation clarity, in the following we omit explicitly stating wavelength dependency.

4.6.1 *Atmospheric Extinction.* For cell initialization with direct sunlight as well as during multiple scattering, we need to compute the attenuation of light traveling through the atmosphere layers. *Source radiant power* $I_{\text{src}}(\lambda)$ (either from the Sun or from a different source cell $C_{\text{src}}$) is attenuated on its way through the atmosphere such that only a fraction arrives at any target cell $C_{\text{tgt}}$. The (wavelength-dependent) extinction factor $\xi_\gamma(\lambda)$ for light traveling along a path $\gamma$ through the atmosphere is equal to

$$\xi_\gamma(\lambda) \;=\; \exp\left(-\int_\gamma \left(\sigma_e^{\text{aerosol}}(\lambda) + \sigma_e^{\text{air}}(\lambda)\right)\,\mathrm{d}s\right)\,. \tag{3}$$

As mentioned in Section 4.1.2, the extinction coefficient of air $\sigma_e^{\text{air}}(\lambda)$ is equal to the scattering coefficient $\sigma_s^{\text{air}}(\lambda)$, whereas the aerosol extinction coefficient $\sigma_e^{\text{aerosol}}(\lambda)$ also includes a contribution from absorption. Since atmospheric extinction varies with altitude, each atmosphere layer $L_i$ is assigned its individual coefficient values $\sigma_{e,i}^{\text{air}}(\lambda)$, $\sigma_{e,i}^{\text{aerosol}}(\lambda)$, and also $g_i(\lambda)$. The light trajectory $\gamma$ from the source to the target cell is traced through the layers, and the extinction factor is numerically determined via

$$\xi_\gamma(\lambda) \;=\; \exp\left(-\sum_{i=1}^{N}\left(\sigma_{e,i}^{\text{air}}(\lambda) + \sigma_{e,i}^{\text{aerosol}}(\lambda)\right)\cdot\Delta\gamma_i(\lambda)\right), \tag{4}$$

where $\Delta\gamma_i(\lambda)$ denotes the path length through layer $i$. Note that, depending on source-target configuration, typically not all layers are traversed, while, on the other hand, it can happen that a single layer is traversed twice due to the Earth's curvature.

To compute the amount of radiant power that is scattered within the target cell $C_{\text{tgt}}$, we compute the intersection points of the light trajectory $\gamma$ with the boundaries of $C_{\text{tgt}}$. Let $\gamma_{\text{front}}$ and $\gamma_{\text{back}}$ denote the paths from the source cell to the front and back intersection points with the target cell, respectively. The radiant power $I_{\text{tgt}}(\lambda)$ scattered by the target cell $C_{\text{tgt}}$ is then determined by

$$I_{\text{tgt}}(\lambda) \;=\; I_{\text{src}}(\lambda)\cdot\left(\xi_{\gamma_{\text{front}}}(\lambda) - \xi_{\gamma_{\text{back}}}(\lambda)\right)\cdot\frac{\sigma_s(\lambda)}{\sigma_e(\lambda)}\cdot\frac{\omega_{\text{tgt}}}{4\pi}\,, \tag{5}$$

with $\sigma_s(\lambda) = \sigma_s^{\text{air}}(\lambda)+\sigma_s^{\text{aerosol}}(\lambda)$, $\sigma_e(\lambda) = \sigma_e^{\text{air}}(\lambda)+\sigma_e^{\text{aerosol}}(\lambda)$ being the scattering and extinction coefficients at the target cell's position, respectively, and $\omega_{\text{tgt}}$ denoting the solid angle of the target cell as seen from the source cell:

$$\omega_{tgt} \;=\; \frac{1}{2}\left(1-\cos\left(\arctan\left(\frac{1}{||C^*_{\text{src}} - C^*_{\text{tgt}}||}\cdot\sqrt{\frac{A_{\text{tgt}}}{\pi}}\right)\right)\right).$$

$A_{\text{tgt}} = V_{\text{tgt}}/(\gamma_{\text{back}} - \gamma_{\text{front}})$ is the projected area of the target cell of volume $V_{\text{tgt}}$. The path length through each layer $\Delta\gamma_{\text{front}}(i)$ as well as the front and back intersection points with the target cell $\gamma_{\text{front,back}}$ is calculated by efficient ray-plane intersection routines.

4.6.2 *Scattering Passes.* To consider the first scattering event in the atmosphere, for each cell $C_k$ we calculate the amount of direct solar irradiance reaching the cell according to Equation (4). The amount of

light scattered inside the cell's volume by air molecules $I_1^{\text{isotr}}$ and aerosols $I_1^{\text{anisotr}}$ is calculated and stored separately (since we model the Sun as a directional light source having irradiance, we substitute for $\omega_{\text{tgt}}/4\pi$ in Equation (5) the cell's projected area $A_{\text{tgt}}$ ). This way, each cell is initialized with the radiant power (in physical unit Watts) received from the Sun that is scattered inside the cell.

Radiative transfer between all pairs of cells is computed assuming isotropic scattering for the air contribution $I_1^{\text{iso}}$ and anisotropic scattering according to Equation (1) for the contribution from aerosols $I_1^{\text{anisotr}}$. For all possible source-target cell pairs, Equation (5) is evaluated, and both contributions from air and aerosol scattering are combined. At each target cell $C_{\text{tgt}}$, the radiant power received from all source cells is accumulated to yield $I_2$ of $C_{\text{tgt}}$.

For the next and all higher-order scattering events, the combined effective isotropic scattering coefficient $(\sigma^{\text{air}} + \overline{\sigma}^{\text{aerosol}})$ is used (Section 4.5.3). We repeat calculating the pairwise energy exchange between all cells by now setting $I_2$ as the source cells' outgoing radiant power. This way, we obtain the contribution to each cell from light that has been scattered three times, $I_3$. This procedure can be repeated arbitrarily many times to take into account as many multiple scattering events as desired. The simulation time growths linearly with the number of scattering events.

To limit memory requirements, it is possible to work with only four buffers per cell: one for the initial anisotropic contribution $I^{\text{anisotr}}$, one for accumulating the total isotropic contribution $I^{\text{isotr}}$, one for the radiant power received during the last pass only $I^{\text{last}}$ (needed next time when acting as source cell), and one for gathering the current incoming radiant power $I^{\text{current}}$. After calculating several passes, $I^{\text{isotr}}$ contains the amount of radiant power that corresponds to the cell's equilibrium state between incoming and outgoing light. Thanks to the atmosphere's relative transparency, $I^{\text{isotr}}(C_k)$ converges quickly to the equilibrium state. Our experiments show that after 5 scattering events, any cell deviates from its equilibrium by much less than 1%, in accordance with results stated in the literature [Blattner et al. 1974; Ougolnikov and Maslov 2002].

## 4.7 Creating the Sky Texture

We now know for each cell $C_k$ the scattered total radiant power $I^{\text{isotr}}(C_k)$ plus the contribution from direct sunlight that has been anisotropically scattered once by aerosol particles, $I^{\text{anisotr}}(C_k)$. To determine sky colors as seen from the observer's position, we calculate the radiance scattered from each cell towards an imaginary detector of unit area at the origin. We consider both contributions $I^{\text{isotr}}(C_k)$, $I^{\text{anisotr}}(C_k)$ separately to correctly account for the singly, anisotropically scattered sunlight by aerosol particles. This is important since it turns out that the aerosol-induced forward scattering ($g > 0$)is responsible for the halo around the Sun. For each hemispherical cell direction (Section 4.1.3), we sum the scattered radiance over all radial shells, taking into account the extinction (Equation (4)) along the path from each cell to the observer.

Having completed the simulation run for several wavelengths in parallel, the spectral radiance distribution is converted to RGB [Wyszecki and Stiles 1982]. We have tested different numbers of wavelengths before we decided to settle for 8 wavelengths ranging between 380 nm and 720 nm. The selected wavelengths yield almost exactly the same visual results as if using 16 wavelengths while considerably reducing computation times.

We typically run our simulation for a spherical environment map with 3° angular resolution. Because sky color varies only slowly with direction, we employ linear interpolation to achieve realistic, high-definition sky textures. Comparative measurements with higher-resolution simulation runs show that virtually no details are lost at 3° intervals.

## 5. OPTIMIZATIONS

A naïve implementation of the described approach results in huge computation times for each multiple scattering pass. The main reason for the high computational costs of multiple scattering is the nested loop: For each (source) cell $C_{\mathrm{src}}$ of the atmosphere model, we loop over all (target) cells $C_{\mathrm{tgt}}$ and compute the radiative transfer between source and target cell. The most expensive procedure within the innermost loop is the computation of the atmospheric extinction along the path from $C_{\mathrm{src}}$ to $C_{\mathrm{tgt}}$ (Section 4.6.1).

To reduce the computational costs of multiple scattering, we can exploit several symmetries. Obviously, the distribution of radiant power in the "left" and "right" part of the atmosphere model is symmetric w.r.t. the direction from the observer to the Sun. Thus, we may loop over only half of all source cells and update two corresponding target cells simultaneously for each source cell. Furthermore, for each pair of one source cell $C_{\mathrm{src}}$ and one target cell $C_{\mathrm{tgt}}$, there is a corresponding pair $(C_{\mathrm{src}}, \overline{C_{\mathrm{tgt}}})$ for which the path from $C_{\mathrm{src}}$ to $\overline{C_{\mathrm{tgt}}}$ is symmetric to the path from $C_{\mathrm{src}}$ to $C_{\mathrm{tgt}}$. $\overline{C_{\mathrm{tgt}}}$ lies symmetric to $C_{\mathrm{tgt}}$ w.r.t. the plane through $C_{\mathrm{src}}$ and the $z$-axis of the local horizontal coordinate system. Hence, the atmospheric extinction computed for the path from $C_{\mathrm{src}}$ to $C_{\mathrm{tgt}}$ can be re-used for the computation of radiative transfer between $C_{\mathrm{src}}$ to $\overline{C_{\mathrm{tgt}}}$, allowing $C_{\mathrm{tgt}}$ and $\overline{C_{\mathrm{tgt}}}$ to be updated simultaneously with only one evaluation of the atmospheric extinction. Combining the two symmetries described above reduces the number of path computations in the nested loop to a quarter of the initial number.

A large reduction in computational cost can be obtained by organizing the loop over all source cells in such a way that all cells on a ring $R$ of constant height within each shell are regarded successively, i.e. the innermost source loop runs over the parameter $\phi$ from Section 4.1.3. In this case, the paths from any one source cell of $R$ to all other target cells are identical if the target cell index is shifted corresponding to the source cell. Thus, we compute all atmospheric extinctions for the first source cell of a ring and store them in a temporary buffer. For all other source cells of the ring, we use the stored extinction factors instead of re-computing them. Actually, we store the extinction multiplied by the solid angle (factor $(\xi_{\gamma_{\mathrm{front}}}(\lambda) - \xi_{\gamma_{\mathrm{back}}}(\lambda)) \cdot \omega_{\mathrm{tgt}}$ in Equation (5)), since the geometry of the atmosphere model is symmetric about the $z$-axis. This optimization reduces the number of path computations by a factor of $S$, with $S$ being the number of cells in one ring, i.e. the number of azimuthal subdivisions.

The above-mentioned optimization steps are purely algorithmic and do not introduce any approximation errors. To further reduce the computational times of multiple scattering, we make use of the observation that the computational cost is dominated by the number of shells. We perform multiple scattering only for a subset of all shells (denoted as *active shells*) and interpolate the other shells (*passive shells*). Both loops over source and target cells benefit from this subsampling. Considering only every $n$-th shell during multiple scattering reduces the number of path computations by a factor of $O(n^2)$. After each multiple scattering pass, the target cells from passive shells are updated using linear interpolation between their neighboring cells from active shells. We have to take into account that only a subset of source cells has been regarded. To ensure a physically correct energy balance, the total amount of energy received by every target cell has to be scaled by the ratio $I_{\mathrm{all}}/I_{\mathrm{active}}$, where $I_{\mathrm{all}}$ and $I_{\mathrm{active}}$ denote the total radiant energy summed over all source cells and over the source cells of active shells only, respectively. We regard every fourth shell during multiple scattering computation, having validated that the obtained results are indistinguishable from complete-shell simulations. This observation can be understood when considering that the optical parameters of the atmosphere vary very smoothly along radial direction In addition, the filtering effect of multiple scattering (diffusion) smears out any localized inhomogeneity.

## 6. RESULTS

Our system is capable of calculating accurate sky maps for a variety of different climates, humidities, and times of the day. All images shown in this paper have been computed with the following parameters:

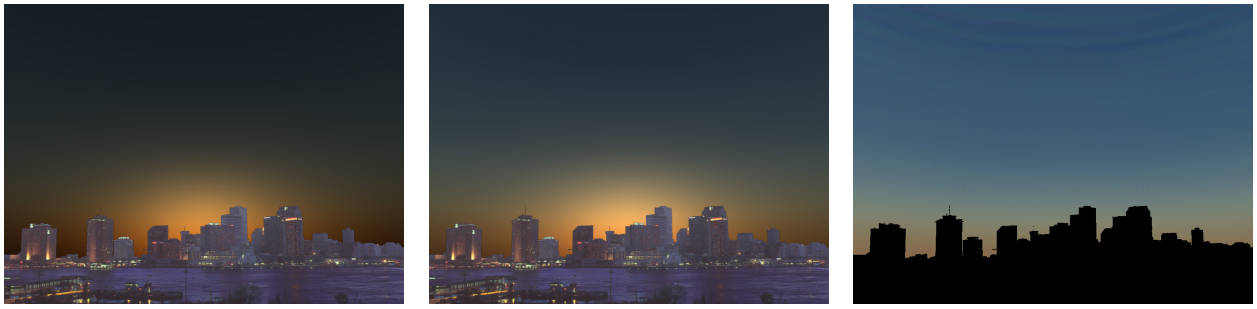

Fig. 7. Importance of multiple scattering for twilight phenomena. Left to right: single scattering (i.e. direct illumination only), multiple scattering with five scattering events, and difference image (gamma-corrected with $\gamma = 3.0$, exaggerating the otherwise invisible concentric atmosphere model structure). For all simulations, a polluted continental climate and a local time of 6:30 pm (DST, sun elevation $+10°$ above the horizon) has been selected.

Fig. 8. Effect of varying humidity on the colors of the sky. Left to right: 50 %, 80 %, and 95 % humidity. All simulations have been performed for the same location, time (6:35 pm DST, sun elevation $+9°$), and type of climate (continental, average pollution).

—color spectra with $N_\lambda = 8$ wavelength samples in the range $[380\,\text{nm}, 720\,\text{nm}]$;

—$N = 50$ atmosphere layers;

—$S = 120$ azimuthal subdivisions (corresponding to a $3°$ angular subdivision);

—multiple scattering with five scattering events.

Computation times are less than two hours[2] on a 3 GHz Intel Pentium4 PC for the complete hemisphere, using up to 100 MB of memory. Once the sky texture has been generated, it can be rendered at real-time frame rates for any viewing direction using standard graphics hardware. For all images shown here, the foreground has simply been added by image composition.

We found the OPAC software [Hess 1998] to be very useful and flexible alike. OPAC readily provides typical aerosol compositions and height profiles for a variety of atmospheric conditions (continental, urban, maritime, desert, (ant-)arctic climate; clean, average, polluted conditions). Besides these pre-defined climates, the user

[2]When profiling our optimized implementation, we found that about 25 % of the total computation time is taken up by evaluating the `exp()` function. Substituting the `exp()` function call by an interpolated table lookup made things even worse: both computation times (due to cache misses) and the approximation error increased.

Fig. 9. Different types of climate. Left to right: continental climate with average pollution, urban climate with heavy pollution, and tropical maritime climate with no pollution. Location, time (6:05 pm DST, sun elevation +15°), and humidity (80 %) is identical for all simulations.

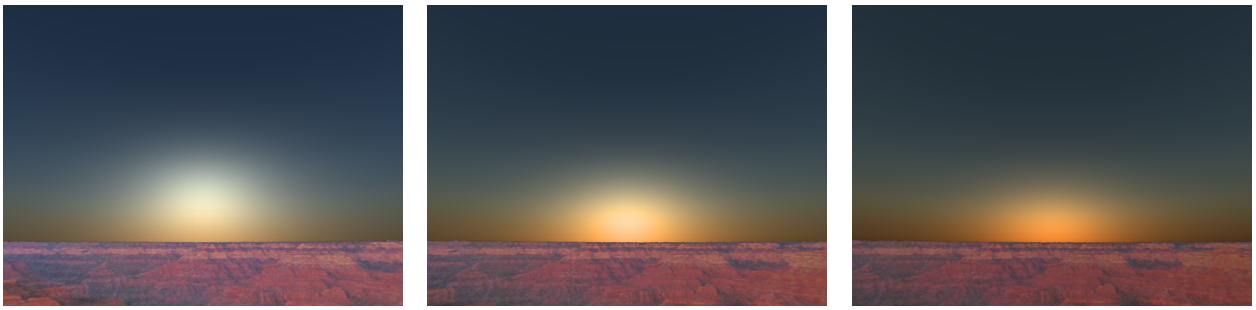

Fig. 10. Sunset sequence for a continental climate with average pollution and 80 % humidity. Left to right: local time 5:30 pm DST (sun elevation +22°), 6:15 pm DST (sun elevation +13°), and 6:40 pm DST (sun elevation +8°).

can define arbitrary aerosol compositions by specifying the density of different types of minerals, soot, sulfates, and fresh or sea-water.

Figure 7 shows the importance of multiple scattering when simulating twilight phenomena. When the Sun is below the horizon, more and more atmosphere cells do not receive any direct illumination, and the sky becomes dark if only single scattering is taken into account. Only due to multiply scattered sunlight do we observe the colorful twilight display ranging over the entire hemisphere. Extensive simulation runs showed that we need to take four scattering events into account if we are to obtain sky map radiance of less than 1 % maximum error. The relative difference in radiance between single scattering and multiple scattering with four scattering events can reach up to about 20 %.

The effect of varying humidity is depicted in Figure 8. The higher the humidity, the more pronounced are the orange-reddish colors during sunset. For continental climate, minute beads of sulfuric acid make up a considerable portion of the aerosol mixture. Due to their hygroscopic nature, the sulfuric acid beads grow in size with increasing relative humidity which changes overall atmospheric scattering and extinction characteristics notably.

Climate conditions differ by the amount and composition of aerosol particles as well as their size and height distribution. This can be witnessed in Figure 9. Despite the same Sun position and relative humidity, twilight sky colors vary considerably. Dust and other aerosols in the lower layers of the atmosphere cause the typical brownish band on the horizon during sunset. The dark horizon and orange sky tint seen from

Fig. 11. Geometric camera calibration: A 15-second exposure of the night sky already reveals the positions of numerous stars. After identifying the constellations, the stars' positions in the image are compared to their azimuth and altitude coordinates computed for the place, date, and time of the exposure. This way, camera orientation, field of view, as well as lens distortion can be recovered.

metropolitan areas occur due to large aerosol concentrations close to the ground. Tropical maritime sunsets far away from industrial pollution are distinguished by their dark blue skies and white-yellowish sun corona.

A sunset sequence for a continental climate is depicted in Figure 10. Color hues and sky brightness vary faithfully as nightfall progresses. All images are rendered by separately mapping image intensity linearly to the output range. To follow sky appearance over the course of a sunset, on the accompanying video virtual exposure time is scaled automatically using mean image intensity in conjunction with appropriate gamma correction. While this approach yields satisfactory results, a more advanced tone mapping operator modeled after the human visual system's mesopic vision characteristics would be desirable.

## 7. VALIDATION

To validate the rendering results, we recorded digital photographs of a late-autumn sunset. The images were taken using a Canon Ixus©digital camera on a tripod on the evening of December 8, 2003, from Saarbrücken, Germany. A series of pictures was taken, covering the entire twilight period from 4:00 pm until 6:00 pm CET in 4-minute intervals. The camera's built-in zoom lens was set to the wide-angle setting. The camera's response curve was later photometrically calibrated in the lab, and the images adjusted accordingly. For calibration, a long-exposure photo was taken after the twilight period had ended, showing a number of stars, see Figure 11. By matching the stars' image coordinates to their calculated azimuth and altitude angles for the date, time and place of the picture, the photo series' field of view and orientation was recovered with arcminute accuracy.

We run our simulation system for the place, date and times of the photographs. The climatic conditions on the ground are available on a half-hourly basis, provided by a meteorological station a few kilometers away from the recording site. For the aerosol distribution and atmospheric height profile, we test the different standard climate conditions provided by OPAC. Two simulation results are depicted along an actual photo of the twilight in Figure 12. Just prior to the recorded sunset, a cold front had passed over central Europe, leaving clear, unpolluted air in its wake. The difference in the sky's blue hue can be attributed to imperfect photometric calibration. Notice, however, the similarity of the orange-red band along the horizon, especially

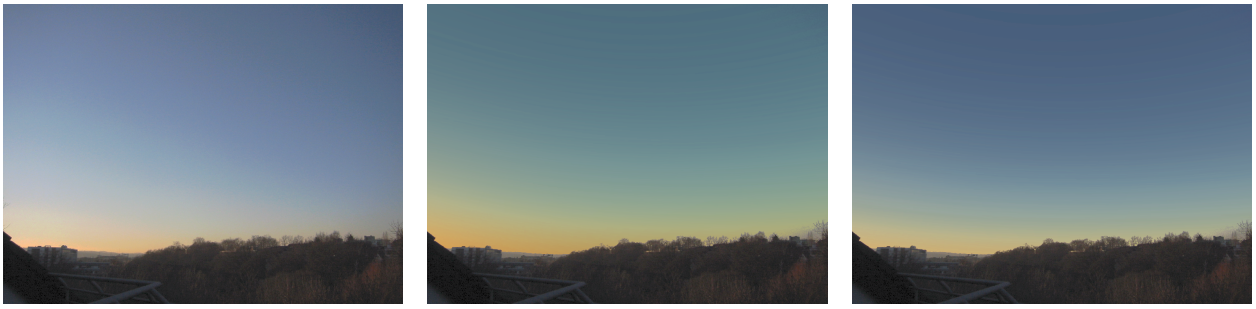

Fig. 12. Left to right: Photograph of a late-autumn sunset after a cold front had passed through. For the same time, place and view as the photo, sunset appearance has been calculated for average continental conditions (middle) and clean continental air (right). For ease of comparison, the photograph's foreground has been added in the simulated views.

in comparison to the simulated sky appearance for clean continental air conditions.

By simulating only a handful of standard atmospheric conditions, the simulation results cannot be expected to be identical to actual photographs. It remains as future work to automatically determine atmospheric model parameters such that twilight renderings match actual twilight recordings. Such a method will be able to serve as a passive, easy to use probing technique, e.g., for atmospheric pollution.

## 8. CONCLUSIONS AND FUTURE WORK

We have presented a physically based rendering algorithm to recreate realistic twilight skies from meteorological parameters, filling the gap between previous daylight and night sky rendering approaches. The influence of sun position and climate conditions on twilight colors is faithfully replicated. Computation times of less than two hours on a conventional PC demonstrate the applicability of the algorithm to a wide variety of photo-realistic rendering scenarios. In addition to rendering vistas of the sky for outdoor scenes, our physically correct, high-dynamic range environment maps of the sky can be used for global illumination computations. At this point, we do not take into account terrain and clouds. Sunlight reflected off the Earth's surface is at most 4 % for ocean surfaces and typically much lower (soil, rock) and can be safely neglected without introducing inaccurate results. Also, some clouds in an otherwise clear sky do not considerably contribute to the amount of scattered radiation in the atmosphere. Shadowing effects, for instance from mountain silhouettes or single clouds, can be easily incorporated into our system's framework simply by treating them as light-absorbing entities in our atmosphere model. Furthermore, cloud appearance can be realistically modeled at low sun elevations by illuminating them in 3D using our atmosphere cells' radiant power distribution.

Based on this work, several research directions will be pursued. We already successfully investigated the rendering of the solar disc taking into account Rayleigh and Mie scattering, atmospheric refraction, and absorption [Linţu et al. 2005]. We wish to validate our simulations results by comparing our rendered images to calibrated photographs of sunsets during known atmospheric conditions. This way, we intend to advance previous work on atmospheric aerosol probing based on twilight measurements [Bigg 1956; Shah 1970; Jadhav and Londhe 1992; Belikov 1996]. The light level during twilight ranges between pure photopic ($3.4\,\mathrm{cd/m^2}$) and scotopic ($0.034\,\mathrm{cd/m^2}$) vision. The psycho-physics of this intermediate range of mesopic vision can be efficiently investigated using our simulation results. By comparing rendered images to actual sunsets, realistic tone mapping operators for mesopic vision may be developed.

## Acknowledgments

The authors would like to thank Dr. Peter Köpke (Meteorologisches Institut, LMU Munich), Dr. Stephan Bakan (MPI Meteorologie, Hamburg), Andrei Lintu (MPI Informatik), and Jeff Schoner (MPI Informatik / UNC Chapel Hill) for their help during this project, and the anonymous reviewers for their valuable comments and suggestions.

## REFERENCES

Adams, C. N., Plass, G. N., and Kattawar, G. W. 1974. The influence of ozone and aerosols on the brightness and color of the twilight sky. *Journal of the Atmospheric Scineces 31,* 6, 1662–1674.

Anderson, D. 1983. The troposphere-stratosphere radiation field at twilight: A spherical model. *Planetary and Space Science 31,* 12, 1517–1523.

Belikov, Y. 1996. Modelling of the twilight sky brightness using a numerical solution of the radiation transfer equation. *Journal of Atmospheric and Terrestial Physics 58,* 16 (Dec.), 1843–1848.

Bigg, E. 1956. The Detection of Atmospheric Dust and Temperature Inversions by Twilight Scattering. *Journal of Meteorology 13,* 3, 266–268.

Blattner, W., Horak, H., Collins, D., and Wells, M. 1974. Monte-Carlo Studies of Sky Radiation at Twilight. *Applied Optics 13,* 3, 534–547.

Bruton, D. 1996. Optical determination of atmospheric temperature profiles. Ph.D. thesis, Texas A&M University.

Chandrasekhar, S. 1950. *Radiative Transfer*. Oxford University Press.

Ciddor, P. E. 1996. Refractive index of air: new equations for the visible and near infrared. *Applied Optics 35,* 9 (Mar.), 1566–1573.

CIE-110-1994. 1994. Spatial distribution of daylight- luminance distributions of various reference skies.

Cohen, M. F., Chen, S. E., Wallace, J. R., and Greenberg, D. P. 1988. A Progressive Refinement Approach to Fast Radiosity Image Generation. In *Computer Graphics (SIGGRAPH '88 Conf. Proc.)*, J. Dill, Ed. Vol. 22. ACM SIGGRAPH, 75–84.

Dave, J. V. and Mateer, C. L. 1968. The effect of stratospheric dust on the color of the twilight sky. *Journal of Geophysical Research 73,* 22, 6897–6913.

Dobashi, Y., Nishita, T., Kaneda, K., and Yamashita, H. 1997. A fast display method of sky colour using basis functions. *The Journal of Visualization and Computer Animation 8,* 2 (Mar.), 115–127.

Gruner, P. and Kleinert, H. 1927. *Die Dämmerungserscheinungen*. Henri Grand, Hamburg.

Hall, R. 1989. *Illumination and Color in Computer Generated Imagery*. Springer, New York.

Heim, A. 1912. *Luft-Farben*. Hofer & Co. AG Graphische Anstalt, Zürich.

Hess, M. 1998. OPAC (Optical Properties of Aerosols and Clouds). available from `ftp://ftp.lrz-muenchen.de/pub/science/meteorology/aerosol/opac/index.ht%ml`.

Hess, M., Koepke, P., and Schult, I. 1998. Optical Properties of Aerosols and Clouds: The Software Package OPAC. *Bulletin of the American Meteorological Society 79,* 5 (May), 831–844.

Irwin, J. 1996. Full-spectral Rendering of the Earth's Atmosphere using a Physical Model of Raleigh Scattering. In *Proc. 14th Eurographics UK Conference*. 103–115.

Jackel, D. and Walter, B. 1997. Modeling and Rendering of the Atmosphere using Mie Scattering. *Computer Graphics Forum 16,* 4, 201–210.

Jadhav, D. and Londhe, A. 1992. Study of Atmospheric Aerosol Loading using the Twilight Method. *Journal of Aerosol Science 23,* 6 (Sept.), 623–630.

Kajiya, J. T. 1984. Ray Tracing Volume Densities. In *Compter Graphics (SIGGRAPH '84 Conf. Proc.)*. Vol. 18. 165–174.

Kajiya, J. T. 1986. The Rendering Equation. *Computer Graphics (SIGGRAPH '86 Conf. Proc.) 20,* 4 (Aug.), 143–150.

Klassen, R. 1987. Modeling the Effect of the Atmosphere on Light. *ACM Transactions on Graphics 6,* 3 (July), 215–237.

Kurucz, R. L., Furenlid, I., Brault, J., and Testerman, L. 1984. Solar Flux Atlas from 296 to 1300 nm. Tech. rep., NOAO, Sunspot, NM. available from `http://kurucz.harvard.edu/sun/fluxatlas/`.

Lilienfeld, P. 2004. A Blue Sky History. *Optics and Photonics News 15,* 6 (June), 32–39.

Linţu, A., Haber, J., and Magnor, M. 2005. Realistic Solar Disc Rendering. In *WSCG'2005 Full Papers Conference Proceedings*. 79–86.

Lynch, D. K. and Livingston, W. 2001. *Color and Light in Nature*. Cambridge University Press, Cambridge.

Magnor, M., Dorn, P., and Rudolph, W. 2001. Simulation of Confocal Microscopy through Scattering Media with and without Time Gating. *Journal of the Optical Society of America B (JOSA B) 18,* 11 (Nov.), 1695–1700.

Max, N. 1994. Efficient Light Propagation for Multiple Anisotropic Volume Scattering. In *Proc. 5th Eurographics Workshop on Rendering)*. Springer Wien, 87–104.

Meeus, J. 1988. *Astronomical Formulae for Calculators*, 4th ed. Willmann-Bell, Richmond, VA.

Meeus, J. 1999. *Astronomical Algorithms*, 2nd ed. Willmann-Bell, Richmond, VA.

Minnaert, M. 1999. *Light and Color in the Outdoors*. Springer, New York.

Nagel, M. R., Quenzel, H., Kwet, W., and Wendling, R. 1978. *Daylight Illumination — Color-Contrast Tables for Full-Form Objects*. Academic Press, New York.

Nimeroff, J., Dorsey, J., and Rushmeier, H. 1996. Implementation and Analysis of an Image-based Global Illumination Framework for Animated Environments. *IEEE Transactions on Visualization and Computer Graphics 2,* 4 (Dec.), 283–298.

Nishita, T., Dobashi, Y., Kaneda, K., and Yamashita, H. 1996. Display Method of the Sky Color Taking into Account Multiple Scattering. In *Proc. Pacific Graphics '96*. IEEE, 117–132.

Ougolnikov, O. and Maslov, I. 2002. Multicolor polarimetry of the twilight sky: The role of multiple light scattering as a function of wavelength. *Cosmic Research 40,* 3 (May), 224–232.

Preetham, A. J., Shirley, P., and Smits, B. 1999. A Practical Analytic Model for Daylight. In *Computer Graphics (SIGGRAPH '99 Conf. Proc.)*. ACM SIGGRAPH, 91–100.

Royal Meteorological Institute of Belgium. 2002. available from `http://www.meteo.be/ozon/ozone/general.php`.

Rozenberg, G. V. 1966. *Twilight: A Study in Atmospheric Optics*. Plenum Press, New York.

Rushmeier, H. and Torrance, K. 1987. The Zonal Method for Calculating Light Intensities in The Presence of a Participating Medium. In *Computer Graphics (SIGGRAPH '87 Conf. Proc.)*. Vol. 21. 293–302.

Shah, G. 1970. Study of Aerosols in Atmosphere by Twilight Scattering. *Tellus 22,* 1, 82–93.

Shirley, P. 1990. Physically Based Lighting Calculations for Computer Graphics. Ph.D. thesis, Dept. of Computer Science, University of Illinois, Urbana-Champaign.

Sloup, J. 2002. A Survey of Modelling and Rendering of the Earth's Atmosphere. In *Proc. 18th Spring Conference on Computer Graphics (SCCG 2002)*. 135–144.

Stam, J. and Languenou, E. 1996. Ray Tracing in Non-Constant Media. In *Rendering Techniques '96 (Proc. 7th EG Workshop on Rendering)*. 225–234.

Tadamura, K., Nakamae, E., Kaneda, K., Baba, M., Yamashita, H., and Nishita, T. 1993. Modeling of Skylight and Rendering of Outdoor Scenes. *Computer Graphics Forum (Proc. Eurographics '93) 12,* 3 (Sept.), C189–C200.

van de Hulst, H. C. 1982. *Light Scattering by Small Particles*. Dover Publications, Inc., New York.

Walker, E. Edward walker's study in the great plains in the winter around 45°n. http://encyclopedia.thefreedictionary.com/Albedo.

Wann Jensen, H., Durand, F., Stark, M. M., Premoze, S., Dorsey, J., and Shirley, P. 2001. A Physically-Based Night Sky Model. In *Computer Graphics (SIGGRAPH 2001 Conf. Proc.)*. ACM SIGGRAPH, 399–408.

Wyszecki, G. and Stiles, W. S. 1982. *Color Science: Concepts and Methods, Quantitative Data and Formulae*, 2nd ed. John Wiley & Sons, New York.